

Design Procedure for Transformer-based Solid-State Pulse Modulators with Damping Network

Spyridon Stathis and Juergen Biela
 Laboratory for High Power Electronic Systems, ETH Zürich
 stathis@hpe.ee.ethz.ch

Keywords

“Pulse Transformer”, “Solid-State Modulator”, “Damping Network”, “Optimization”, “Varistor”, “Mineral oil”

Abstract

This paper presents a systematic procedure for designing transformer-based solid-state pulse modulators, which include a damping network at the load side in order to minimize the rise time and the overshoot of the pulse. The design procedure is applied to the specifications of the CARM modulator system to evaluate its performance.

1 Introduction

In many particle accelerator facilities ultra-precise voltage/current pulses with fast rise and settling times with a high flat-top stability and a low overshoot are required. To generate such pulses, often solid-state pulse modulators are used and pulse transformer-based modulator concepts have proven to be able to meet strict pulse requirements [1–3]. For the design of such systems, optimization procedures have been developed [3–5] and as the specifications of the pulses become more and more demanding, a detailed design procedure is inevitable for a reliable prediction of the pulse performance, before the modulator is built.

An example of such a modulator with challenging requirements is the CARM modulator, a mm-wavelength source, which is currently under development at ENEA research center with the specifications listed in Table I [6]. The definitions of the main transient characteristics of the pulse are also given in Fig. 1a). In [7], a first feasibility study is presented for this modulator based on an optimization procedure. This analysis showed that a damping network (DN) arrangement at the load side is mandatory for a good pulse performance as the transformer parasitics result in unwanted resonances. The optimization routine allowed a comparison between different DN types and one DN type proved to be a promising configuration for the specifications of the CARM modulator (Fig. 1b). The optimization routine combined the design of the pulse transformer and the damping network, and it resulted in a preliminary set of transformer parasitics and damping network parameters for an optimal pulse performance.

However, in [7] an ideal behaviour for the operation of the metal-oxide varistors (MOVs) in the DN has been assumed and only a very small parameter range has been considered in the optimization. In order to improve the accuracy of the optimization procedure, a detailed model of the varistor branches is presented in this paper, so that the full potential of the DN and its effect on the transient characteristics of the pulse can be examined. Many

Table I: CARM modulator specifications

Symbol	Parameter	Value	
V_{gun}	Pulsed voltage	700 kV	Electrical pulse parameters
I_{gun}	Pulsed current	8 A	
P_{gun}	Pulsed power	5.6 MW	
t_{flat}	Pulse length	5 μ s	
t_{rise}	Rise time (50%–100%)	$\leq 1 \mu$ s	
t_{settling}	Settling time	$\leq 5 \mu$ s	
os	Overshoot	$\leq 1\%$	
FTS	Flat-top stability	$\leq 0.1\%$	
ΔV	Ripple	$\leq 0.1\%$	
f_{rep}	Repetition frequency	10 Hz	
C_{gun}	Gun capacitance	100 pF	Gun parameters
R_{gun}	Gun resistance	87.5 k Ω	

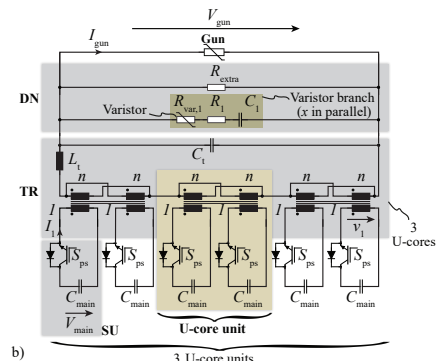
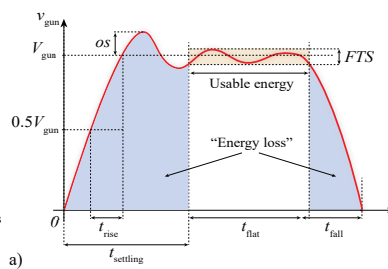


Fig. 1: Table I lists the main specifications of the CARM modulator. a) Indicative voltage pulse shape and definitions of the transient quantities. The energy during t_{settling} and t_{fall} can not be used by the application (“energy loss”). Once the pulse lies within FTS the flat-top interval t_{flat} starts. b) Electrical equivalent circuit of the CARM modulator consisting of 3 U-core units, the pulse transformer (TR) with its total parasitic inductance L_t and capacitance C_t , the damping network (DN) and the gun.

Table II: Considered degrees of freedom & parameters for the transformer optimization

Symbol	Parameter	Value	
d_h	HV side distance	$90 \text{ mm} \leq d_h \leq 190 \text{ mm}$	
d_l	LV side distance	$5 \text{ mm} \leq d_l \leq 20 \text{ mm}$	
d_c	Core depth	$140 \text{ mm} \leq d_c \leq 180 \text{ mm}$	
$h_{2,\text{add}}$	Additional secondary winding height	$10 \text{ mm} \leq h_{2,\text{add}} \leq 100 \text{ mm}$	5 degrees of freedom
d_f	Field ring radius	$8 \text{ mm} \leq d_f \leq 15 \text{ mm}$	
B_{ap}	Applied flux density	1.5 T	
$d_{pc,\text{hor}}$	Horizontal distance core & primary winding	4.5 mm	
$d_{pc,\text{vert}}$	Vertical distance core & primary winding	15 mm	
$d_{ct,\text{bottom}}$	Bottom distance core & tank	15 mm	
$d_{ct,\text{top}}$	Top distance core & tank	50 mm	
d_{rings}	Distance between rings	45 mm	
d_{ft}	Distance field ring & tank	$d_h + 40 \text{ mm}$	
d_2	Thickness of secondary winding turn	2 mm	
d_s	Secondary winding turns distance	1 mm	
d_{cores}	Distance between cores	30 mm	
ϵ_{oil}	MIDEL oil relative permittivity	3.2	
t_r/t_f	IGBT rise/fall time	200 ns	
C_{divider}	HV divider capacitance	50 pF	
L_{gen}	SU parasitic inductance	100 nH	

Fig. 2: a) 2D representation of the oil immersed split-U-core transformer and tank. A tilted secondary winding is realised for minimum leakage inductance [11]. Table II summarizes the degrees of freedom and additional considered parameters for the CARM transformer optimization. The degrees of freedom are shown with red in Fig. 2a).

MOVs models have been proposed in literature. For instance, in [8], the MOV is modelled as a non-linear resistor, which results only in a static model. More realistic models include the parasitic inductances and capacitances [9] as well as the hysteresis of the MOV [10], what results in dynamic models. In this work, a dynamic model for the MOV, including its parasitics, is integrated in the optimization procedure. For validating the accuracy of the transformer models, 3D FEM simulations of the pulse transformer are also performed. The FEM results are used to validate the scaling lengths, which are used for scaling the per unit length parasitic inductance and capacitance in the optimization. In addition, the analytical calculation of the maximum E-field of the transformer geometry is validated with FEM simulations.

The structure of the paper is as follows: In section 2, the optimization routine is discussed with focus on the DN modeling and the suggested improvements on the transformer models. In section 3, results for the CARM transformer design and the enhanced DN modelling are presented. Finally, section 4 summarizes the main outcomes of this work.

2 System Optimization Procedure

The optimization procedure shown in Fig. 3, is based on the procedure presented in [7]. The red frames illustrate the additional improvements and extensions proposed in this paper. The main extension of the routine is the enhanced DN model in the damping network design section. In step S3, the maximum E-field outside of the core window is also taken into account besides the maximum E-field inside the core window. An additional extension is the transformer 3D FEM simulations, which improve the modeling of the parasitics (S5). A representation of the considered 2D transformer geometry is shown in Fig. 2a). Table II provides the degrees of freedom and additional parameters, which were considered during the optimization of the CARM modulator.

2.1 Transformer Design

The procedure starts (S1) by setting the ranges of the 5 degrees of freedom, the pulse specifications as well as some predefined geometrical quantities (Table II). Next, the core dimensions are calculated, which result in the tank and the transformer volume, and in a minimum height for the secondary winding $h_{2,\text{min}}$ (S2). Finally, the secondary winding height h_2 is controlled by the relation $h_2 = h_{2,\text{min}} + h_{2,\text{add}}$. For determining the cross-sectional area of the core, the volts-seconds of the pulse and the allowed saturation flux density are used.

The procedure continues with the calculation of the maximum E-field inside the core window $E_{\text{max},\text{IW}}$ and the maximum E-field outside of the window $E_{\text{max},\text{OW}}$ (S3). Both E-field values are considered because the maximum E-field outside of the core window might be even higher than the E-field inside the core window as FEM simulations revealed. For the analytical calculation of the E-field, the charge simulation method (CSM) is applied [12]. According to [13], a limit of $E_{\text{th}} = 20 \text{ kV mm}^{-1}$ is suitable for short pulse lengths and for mineral oil as an insulating material. However, in particle accelerator facilities, there is a rising demand to replace the mineral oil with more eco-friendly oils such as natural esters [3, 14]. Therefore, the synthetic ester oil Midel 7131 has been selected for the design of the ENEA transformer. In [15], it has been shown that the insulating strength of Midel 7131 is lower than mineral oil under standard impulse conditions (1.2/50 μs). The aging of the oil also affects its insulating strength. Consequently, a more conservative threshold value of 18 kV mm^{-1} is used in the optimization presented

in this paper. For evaluating the impact of the oil on the transformer design, two more cases are considered with a mineral oil and a $E_{\text{th}} = 20 \text{ kV mm}^{-1}$ and $E_{\text{th}} = 25 \text{ kV mm}^{-1}$.

The extraction of the total secondary-referred winding resistance R_{wdg} follows in step S4. The winding losses due to the skin and the proximity effect have been studied extensively in [16] for foil and round conductors. Here, it is assumed that both windings cover the entire core window height. In order to simplify the model, a trapezoidal current shape is assumed with a rise and fall time time of $1 \mu\text{s}$, a flat-top of $5 \mu\text{s}$ and a repetition frequency of $f_{\text{rep}} = 10 \text{ Hz}$ [7]. Using Fourier series, this current is analyzed with 100 harmonics in order to calculate the skin depth. The secondary round turns are transformed to a sheet conductor for calculating the proximity effect losses as described in [16].

Afterwards, the transformer leakage inductance L_{σ} and the distributed capacitance C_d , referred to the secondary side, are calculated in step S5. For analyzing the transformer parasitics, the geometry is simplified by approximating the primary winding with N_2 circular conductors equally distributed along the height of the primary winding. Also, a homogeneous current and voltage distribution is assumed in the parasitics calculation. The influence of the grounded tank and the grounded core is taken into account. For calculating the distributed capacitance per unit length inside and outside the core window the charge simulation method (CSM) is used [12]. For determining the parasitic inductance per unit length inside and outside the core window, the mirror current method is applied according to [17]. In [18], a more accurate model is proposed where an additional elementary cross section between the cores was introduced and this is used to improve the leakage inductance model. The per unit length quantities are then scaled with the appropriate scaling lengths for the inside and the outside core window areas as suggested in [18]. Finally, the total parasitic inductance L_t and capacitance C_t are determined by

$$L_t = L_{\text{gen,s}} + L_{\sigma} \quad C_t = C_d + C_{\text{extra}}$$

There, $L_{\text{gen,s}}$ is the parasitic inductance of the switching unit S_{ps} referred to the secondary side (Fig. 1c) and C_{extra} is the sum of the gun capacitance C_{gun} and the capacitance of the HV divider C_{divider} , which is used for measuring the gun voltage. In step S6, the total parasitic inductance and capacitance, the resistance of the windings, the maximum E-field and the respective values of the degrees of freedom are stored. With the stored values, the pareto front of the transformer parasitics is obtained and a design point with minimal transformer parasitics on the knee of the pareto is selected, which results in the fastest rise time. This method is used to drastically reduce the computational effort of the complete optimization procedure as it allows for a more extensive parametric sweep across the DN parameters of the DN design section [7]. For validating the transformer routine, the models have been also applied to the specifications of the SwissFEL modulator at Paul Scherrer Institute (PSI) [2] and to the CLIC modulator for European Organization for Nuclear Research (CERN) [19] and the measured values have been compared to the calculated ones.

2.2 Transformer Design Check

For the validation of the models for the transformer parasitics as well as the maximum E-field inside and outside the core window several design points have been examined. The validation is performed with automated 3D FEM simulations, which allow to compare L_{σ} , C_d , and E_{max} with the results from the analytical calculations resulting from steps S3 & S5. For the analytical calculation of the transformer parasitics in the optimization, 2D models are used resulting in per unit length quantities and they are multiplied by the associated scaling lengths to get the final 3D values. Therefore, the 3D FEM simulations serve as a reference point in order to verify whether the per unit length leakage inductance and distributed capacitance have been scaled with the appropriate scaling lengths inside

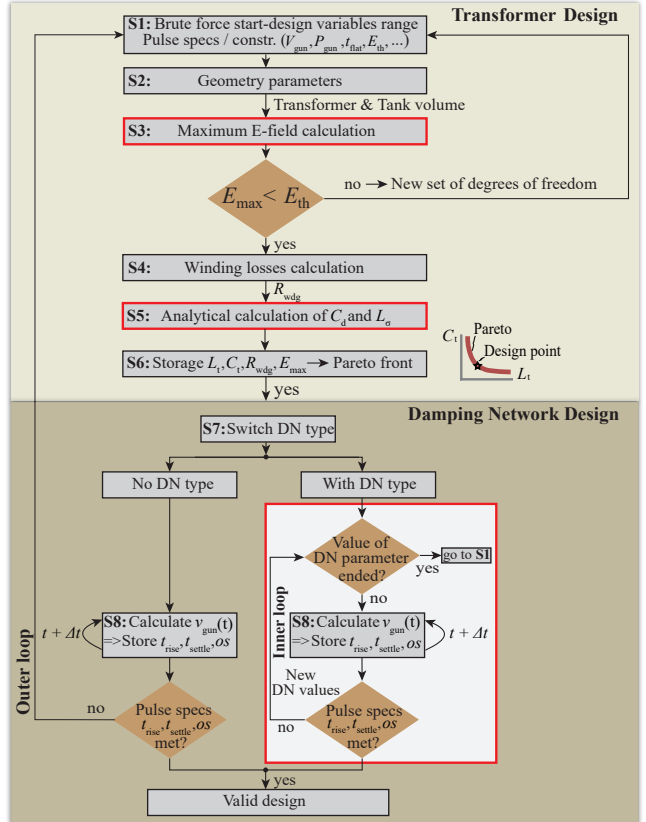


Fig. 3: Flowchart of the optimization procedure including the transformer design and the damping network design. The red frames indicate the improvements of the routine.

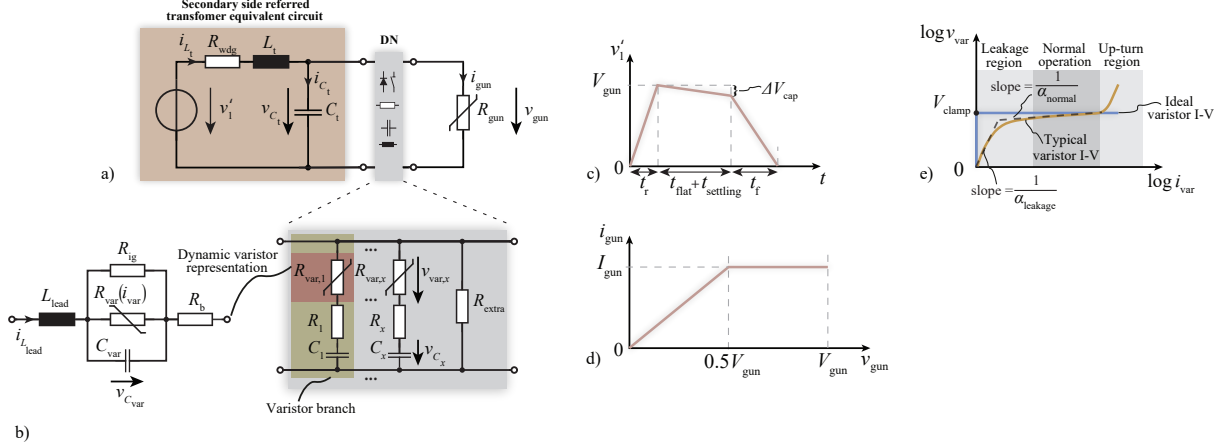


Fig. 4: a) Simplified representation of the transformer and the switching unit including a damping network referred to the secondary side of the transformer. b) Damping network for the CARM modulator. Varistors are placed in series with RC components forming a varistor branch. On the left side, the dynamic varistor representation including its parasitics is provided. c) Voltage signal generated by the switching unit referred to the secondary side, which emulates the switching and the steady behaviour of the switching unit. The IGBT has rise time of t_r and a fall time t_f as given in Table II. d) Current-voltage characteristic of the gun. e) Ideal and typical varistor current-voltage characteristic. The typical I-V characteristic can be approximated by straight lines with different slopes for each operating region.

the optimization and how large the deviation between analytical and 3D FEM values is. With this, the validity of the pareto curve is ensured.

2.3 Damping Network Modeling

With the validated transformer design, the DN is optimized in the next stage (S7 & S8) with a model for the transient behaviour. The dynamic behaviour of the transformer and the switching unit is modeled by the network given in Fig. 4a), which is a simplified representation referred to the secondary side of the transformer. There, v_1' is the primary winding voltage v_1 referred to the secondary side (Fig. 4c). The voltage v_1 is a linear approximation of the switching and steady state of the IGBT with a rise time t_r and a fall time t_f . An additional slope ΔV_{cap} during the time interval $t_{flat} + t_{settling}$ is considered, which emulates the voltage droop of the main capacitors C_{main} during the pulse [7]. This voltage droop results in a more limited flat-top stability FTS_{lim} , which is given as $FTS_{lim} = FTS - \Delta V_{cap}\%$, with FTS being defined in the specifications of Table I. The value of C_{main} should be chosen, so that $\Delta V_{cap}\% \ll FTS$ to limit the influence of the droop on the pulse shape. A possible droop compensation is not considered in this paper in order to simplify the analysis. Moreover, the magnetizing inductance as well as the iron losses are not taken into account as they have insignificant impact due to the short pulse length [11]. The gun has a non-linear current-voltage characteristic, which is depicted in Fig. 4d). The network for the pulse modulator is solved analytically for different types of DN and also for the case without DN (S8), in order to compute the gun voltage v_{gun} during the pulse (S9). A first comparison between different DN types has been made in [7] and, for the CARM modulator, the DN arrangement shown in Fig. 4b) was proved to be promising. In the considered DN type, varistors are placed in series to a RC circuit forming a varistor branch. Multiple varistor branches can be connected in parallel. In addition, an extra resistor R_{extra} should be added to increase the damping as the gun by itself presents a quite high impedance [7].

For achieving a reliable design optimization, a detailed model of the DN is required. In the following, it is considered that the varistors of the parallel branches could have different clamping voltages so that the varistor branches kick in at different voltage levels. There, a dynamic model of the varistor is crucial in order to examine its effect on the transient voltage pulse. For deriving the dynamic varistor model, the typical I-V characteristic of a varistor is used (Fig. 4e), where three operating regions can be identified: the leakage, the normal operation, and the up-turn region [20]. The equivalent circuit of a varistor, which includes the parasitics, is depicted in Fig. 4b). In the varistor model, L_{lead} models the parasitic inductance of the leads, C_{var} is the capacitance of the varistor, $R_{var}(i_{var})$ is the non-linear resistance, which depends on the current that flows through the varistor, R_{ig} models the resistance of the intergranular boundary, and R_b is the bulk resistance of the zinc oxide [20].

For the leakage region, R_{ig} dominates ($R_{ig} \approx 10^9 \Omega$) over $R_{var}(i_{var})$. Consequently, L_{lead} and the parallel combination of C_{var} and R_{off} form essentially the equivalent circuit. In the normal operation region, the varistor conducts and $R_{var}(i_{var})$ dominates now over R_{ig} so that L_{lead} and R_{var} form the equivalent circuit of the varistor. Although the bulk resistance of the zinc oxide is very low ($R_b \approx 1\Omega$), it is included in the model as many varistors are expected to be connected in series, which will, eventually, increase the resistance. The current that flows through the non-linear

resistor $R_{\text{var}}(i_{\text{var}})$ in the normal operating region follows a power law equation $i_{\text{var,normal}} = k_{\text{normal}} v_{\text{var}}^{\alpha_{\text{normal}}}$, where k_{normal} is a constant and α_{normal} is also a constant, which defines the degree of non-linearity, and which is basically the slope of the I-V characteristic. It can be determined by choosing two operating points on the I-V characteristic of the selected varistor component. By performing measurements at varistor components, the authors of [21] showed, that the current in the leakage region can also be approximated by a similar power law relation as for the normal operating region, namely by $i_{\text{var,leakage}} = k_{\text{leakage}} v_{\text{var}}^{\alpha_{\text{leakage}}}$. By adding these two currents a combined model results, which models the behaviour of the varistor in the leakage and the normal region. Hence,

$$i_{\text{var}} = i_{\text{var,leakage}} + i_{\text{var,normal}} = k_{\text{leakage}} v_{\text{var}}^{\alpha_{\text{leakage}}} + k_{\text{normal}} v_{\text{var}}^{\alpha_{\text{normal}}} \quad (1)$$

where v_{var} is the varistor voltage, which is equal to the voltage across the varistor capacitance C_{var} . The four constant parameters of the power law functions are determined through curve fitting. At high currents, in the kA range, the varistor is in the up-turn region. However, in the considered CARM modulator, the varistors are not intended to operate at such high currents so that this region is not considered in the model. It should also be noted that this model ignores the hysteresis loop of varistors [22]. When the surge across the varistor vanishes, the current rapidly drops, but it follows a different path on the I-V curve creating a hysteresis loop. This phenomenon is not modeled as the focus is on the rising edge and there the hysteresis does not play any role.

The capacitance C_{var} is usually provided in the data-sheets at a specific frequency, e.g. at 1 MHz. Also, R_{ig} is known to be in the range of $R_{\text{ig}} \approx 10^9 \Omega$ and remains in the MΩ range even at elevated temperatures whereas R_b is usually in the range of approximately 1 Ω. However, the parasitic inductance L_{lead} is typically not provided in the data-sheets. As typically the focus is on the normal operating region, many data-sheets do not provide the I-V characteristic during the leakage mode of operation. This data limitation becomes more significant for high voltage varistors where the leakage region is often completely neglected. To lift these limitations, and in order to show the modeling procedure, a specific radial-lead varistor is chosen for the damping network design, which offers data for a broader current range from μA to kA. The lead inductance of a radial-lead varistor, which is in fact the self-inductance of a loop of wire, can be calculated by [21]

$$L_{\text{lead}} = \frac{\mu_0 h}{\pi} \ln \left(\frac{d - t_w}{t_w} \right) \quad (2)$$

where μ_0 is the relative permeability of free space, h is the height of the radial leads, d is the distance between the wires and t_w is the thickness of the wire. The geometrical quantities of the considered varistor are extracted through the data-sheet. On a system level, multiple varistors are connected in series in each varistor branch as the estimated clamping voltages of each branch are in the range of half of the gun voltage (350 kV) and above. The number of the varistors $N_{\text{var},x}$, which should be connected in series at the branch x is determined by the relation

$$N_{\text{var},x} = \text{ceil} \left(\frac{V_{\text{var},x}}{V_{\text{clamp}}} \right) \quad x \in \mathbb{Z}^+ \quad (3)$$

where V_{clamp} is the maximum nominal clamping voltage of the selected varistor, $V_{\text{var},x}$ is the clamping voltage of the x varistor branch, i.e. the voltage where all the varistors in series enter the normal operating region. Consequently, the resistances and inductances for the equivalent varistor network have to be multiplied by $N_{\text{var},x}$ and the capacitance has to be divided by the same number. However, radial-lead varistors do not show high clamping voltages and therefore, hundreds of varistor components must be connected in series for the damping network, what results in a reduced reliability of the system. For the real CARM modulator system, varistors with higher voltage ratings will be used and the parasitics could be measured, for example, with an impedance analyzer.

The clamping voltage of the varistor depends on the rise time and the decay time of the applied current waveform [20]. The value of V_{clamp} is usually given in the datasheets for an applied current pulse with a rise time of 8 μs and a decay time of 20 μs (8/20 μs), which has quite a different slope compared to the desired 1 μs rise time waveform for the considered ENEA modulator. According to [20], the clamping voltage tends to increase with a shorter rise and decay time of the applied current pulse. Although this increase of V_{clamp} becomes more severe in the kA range, it also influences the operation at lower currents in the normal operating region. The dependency of the clamping voltage on the waveform of the applied current is typically not provided in the data-sheets. However, in [20], I-V curves for applied current impulses of 1/3 μs, 0.5/1.5 μs and 8/20 μs for a radial-lead varistor in the normal operating region are given. The leakage region remains approximately unchanged by the different current slopes. If one compares the maximum clamping voltage at 100 A (at this current the clamping voltage is typically provided in the data-sheet) for the 1/3 μs pulse, which has approximately the same slope as the desired voltage pulse of the modulator, with the reference 8/20 μs curve, it can be found that there is an increase of around 6% of the clamping voltage. Then, the parameter α_{normal} of equation (1) should show a decrease of around 6% as the

slope of the I-V characteristic is in fact the inverse value of α_{normal} (Fig. 4e). This value has been considered in the modeling for the additional increase of the V_{clamp} . The response time of a varistor is in the range of a few ns [20], which is not comparable to the required rise time of the voltage pulse, and consequently, it does not affect the rise time of the gun voltage.

One should set the differential equations of the system, which is used to solve with respect to the gun voltage v_{gun} , which is equal to v_{C_t} . In order to explain the modeling procedure, the case of a single varistor branch with a clamping voltage $V_{\text{var},1}$ is used as a reference. Applying the voltage/current equations to the circuit of Fig. 4a) and taking into account the equivalent circuit of the varistor in Fig. 4b), one can derive the set of differential equations for the respective state vector \bar{x}_1

$$\bar{x}_1 = [i_{L_t}, v_{C_t}, i_{L_{\text{lead}}}, v_{C_{\text{var}}}, v_{C_1}]^T \quad (4)$$

$$\frac{di_{L_t}}{dt} = \frac{1}{L_t} [v'_1 - i_{L_t} R_{\text{wdg}} - v_{C_t}] \quad (5)$$

$$\frac{dv_{C_t}}{dt} = \frac{1}{C_t} \left[i_{L_t} - i_{L_{\text{lead}}} - \frac{v_{C_t}}{R_{\text{extra}}} - i_{\text{gun}} \right] \quad (6)$$

$$\frac{di_{L_{\text{lead}}}}{dt} = \frac{1}{N_{\text{var},1} L_{\text{lead}}} [v_{C_t} - v_{C_{\text{var}}} - i_{L_{\text{lead}}} (R_1 + N_{\text{var},1} \cdot R_b) - v_{C_1}] \quad (7)$$

$$\frac{dv_{C_{\text{var}}}}{dt} = \frac{1}{N_{\text{var},1}^{-1} C_{\text{var}}} \left[i_{L_{\text{lead}}} - \frac{v_{C_{\text{var}}}}{N_{\text{var},1} R_{\text{ig}}} - \left(k_{\text{leakage}} v_{\text{var}}^{\alpha_{\text{leakage}}} + k_{\text{normal}} v_{\text{var}}^{\alpha_{\text{normal}}} \right) \right] \quad (8)$$

$$\frac{dv_{C_1}}{dt} = \frac{1}{C_1} i_{L_{\text{lead}}} \quad (9)$$

with $v_{\text{var}} = v_{C_{\text{var}}} / N_{\text{var},1}$ due to the serial connection of the varistors.

After calculating v_{gun} , the transient characteristics of the pulse, such as rise time, overshoot and settling time can be computed and stored (S8). The rise time t_{rise} and the overshoot os are defined as

$$t_{\text{rise}} = t_{100} - t_{50} \quad os = \left(\frac{V_{\text{gun,max}}}{V_{\text{gun}}} - 1 \right) \cdot 100\% \quad (10)$$

To calculate the rise time (50%-100%) of the pulse, the points in time t_{50} and t_{100} are used, which indicate the time instances where the voltage pulse reaches 50% and 100%, respectively, of its rated value. In order to compute the overshoot, the maximum gun voltage $V_{\text{gun,max}}$ is determined and the os is compared to the acceptable overshoot given in the specifications. The settling time ends when the voltage pulse lies completely within the *FTS* band. By stepping through v_{gun} in the time domain, the settling point in time is obtained. To limit the calculation time of the optimization, the non-linear set of differential equations (5)-(9) is solved only for the time interval of $t_{\text{control}} = t_{\text{settle}} + t_{\text{add}}$, where $t_{\text{settle}} = 5\mu\text{s}$ is set by the application and $t_{\text{add}} = 2\mu\text{s}$ is chosen, which is a margin to ensure that the pulse will remain safely within the *FTS* limits.

The dependencies between the transient characteristics are investigated via a parametric sweep across the quantities R_1 , C_1 , R_{extra} , $V_{\text{var},1}$, and at the end, the designer can choose the best set of DN parameters for an optimized pulse performance. The same procedure is basically applied in the case where more varistor branches are connected in parallel to the load. There, the set of differential equations is expanded accordingly depending on the number of the parallel varistor branches.

3 CARM Modulator Feasibility Study

The procedure presented in section 2 is applied to the specifications of the CARM modulator, which are listed in Table I, to verify the effectiveness of the optimization routine.

3.1 Transformer Design

The optimization procedure is set to run with the considered degrees of freedom and parameters as shown in Table II. In [7], different number of cores were examined, and a 3-core transformer was found to give a good compromise between the transformer parasitics, the transient performance of the output pulse and the complexity of the system. This, still holds true for the improved optimization routine presented in this paper. Therefore, 3-core transformers are considered in the following. The resulting optimal points and the pareto front of the transformer parasitics are shown in Fig. 5a) in dependency of the maximum E-field. From the pareto front a design point is selected at the knee of the curve, for minimum parasitics, which result in a minimum rise time. The chosen design point results in

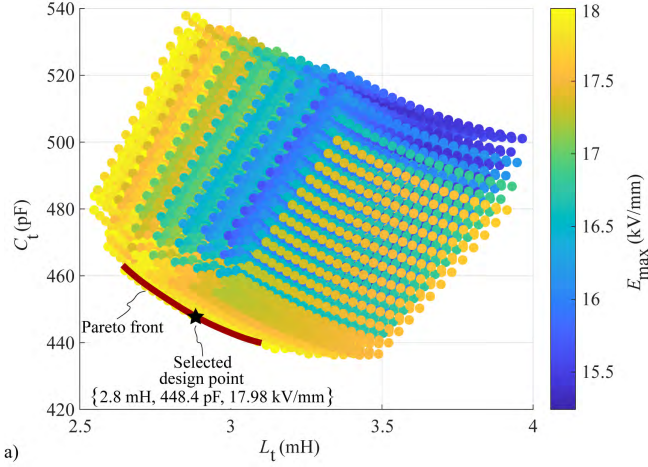


Table III: Parameters of the selected transformer design point		
Symbol	Parameter	Value
d_h	HV side distance	135 mm
d_l	LV side distance	5 mm
d_c	Core depth	140 mm
h_2	Secondary winding height	204.6 mm
d_f	Field ring radius	13 mm
N_c	Number of cores	3
N_2	Secondary winding turns	78
N_1	Primary winding turns	1
A_c	Core cross-sectional area	0.0125 m ²
w_w	Core window width	376 mm
h_w	Core window height	367.6 mm
b_{leg}	Core leg breadth	89.3 mm
h_1	Primary winding height	337.6 mm
w_{tank}	Tank width	1.24 m
h_{tank}	Tank height	0.61 m
l_{tank}	Tank depth	1.16 m

Fig. 5: a) Total parasitic capacitance C_t versus total parasitic inductance L_t in relation to the maximum E-field for a transformer with $N_c = 3$ cores. The red curve indicates the pareto front, where a design point (“★”) is selected. The lower the L_t the higher the E_{\max} becomes. Table III lists some of the main parameters of the selected design point.

a tank and a transformer geometry with the parameters listed in Table III. It is worth mentioning that the maximum E-field occurs on the surface of the field ring outside the core window, a fact which proves the importance of including the calculation of the maximum E-field outside the core window area also in the optimization. Fig. 5a) also clearly demonstrates that the lower the parasitic inductance, the higher E_{\max} becomes given that the distances between the windings tend to be shorter.

3.2 Transformer Design Check

For validating the transformer design, the parasitics and the maximum E-field for the chosen design point are checked via electrostatic and magnetostatic 3D FEM simulations, and the results are compared to the analytical ones of the optimization procedure. All the calculated values are listed in Table IV. For the simulations half of the transformer and the tank geometry is simulated. This helps to investigate the electric and magnetic energy contribution of the region between the cores as well as potential interactions between both secondary windings inside the core window. The FEM simulations are set in such a way so that the calculation of the parasitics inside the core window is feasible. With the 3D simulations as a reference, it is clear that the deviation of the parasitic capacitance C_d is kept below 5% between the 3D simulations and analytical calculations. However, the calculation of L_σ shows a higher value. For the analytical leakage inductance calculation, the model proposed in [18] was used, which increases the accuracy compared to the model used in [3]. The main contributor to the error is the leakage inductance outside of the core window area where an error of 11% error results for the simulated design. For the inside window area the error of the leakage inductance is around 7%. The electrostatic simulations confirm that the maximum E-field lies outside the core window and not inside the window as it is the case for the designs presented in [2, 3]. The maximum E-field is around 18.53 kV mm^{-1} . The maximum E-field inside the core window tends to be lower as the electric field of the two field shape rings superpose each other resulting in a lower total field. This indicates that the optimization procedure has to take into account the maximum E-field outside the window as well and not only the inside window as proposed in [3]. In addition, in Fig. 6, the norm of the E-field and H-field are visualized with three 2D cuts.

3.3 Damping Network Design

in the next step, the damping network is designed following the modeling procedure described in section 2.3. For the DN model, the radial-lead varistor V25S750P of UltraMOV25S series from Littelfuse is selected as example, since data on the different operating regions is provided for this device. The main parameters of the varistor are given in Table V. According to (2), the exact number of the varistor components, which must be connected in series, depends on the chosen varistor clamping voltage $V_{\text{var},x}$. The considered ranges of all the parameters of the

Table IV: Comparison of the parasitics & peak E-field values between 3D FEM and analytical calculation for the selected transformer design

Parameter	Analytical	3D-FEM	Error: Analytical vs 3D
$C_d(\text{pF})$	298.4	285.6	-4.49 %
$L_\sigma(\text{mH})$	1.9	1.61	-18.1 %
$E_{\max} (\text{kV/mm})$	17.98	18.53	2.97 %

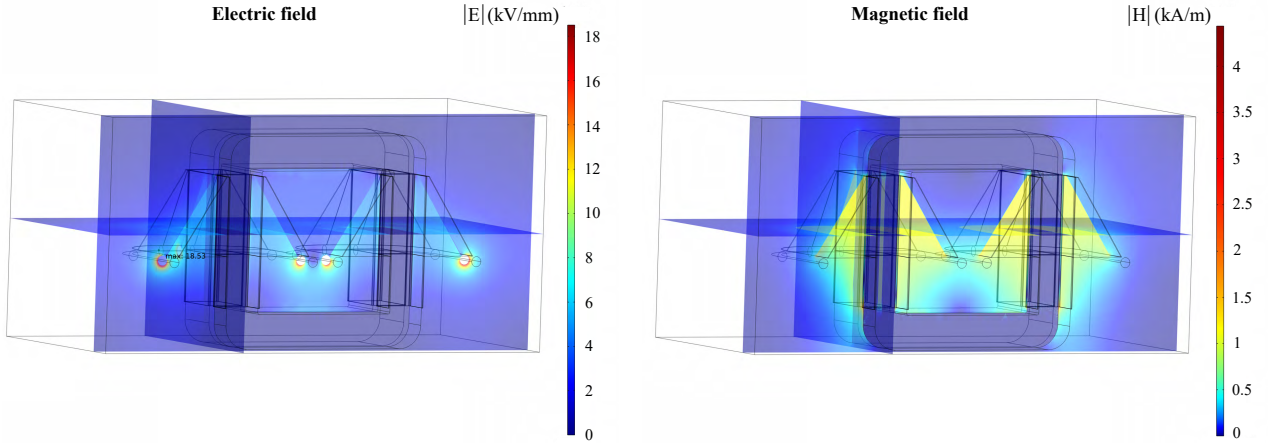


Fig. 6: 3D FEM results for the selected transformer design point with three 2D cuts: a) Norm of the E-field in kV mm^{-1} . The maximum E-field appears on the surface of the field ring outside of the core window. b) Norm of the magnetic field in kA m^{-1} .

DN are provided in Table VI. With a parametric sweep, the best set of these parameters is identified for an optimal pulse performance.

Based on the parameter ranges and the parasitics for the selected design point, the dependency between the rise time and the overshoot can be determined for different number of varistor branches N_b in parallel and clamping voltages $V_{\text{var},x}$ as depicted in Fig. 7. The results indicate that a single varistor branch ($N_b = 1$) does not provide sufficient damping to the output voltage pulse at the $1 \mu\text{s}$ rise time limit. The damping is significantly improved by adding one additional branch in parallel ($N_b = 2$) as it can be seen in Fig. 7b). There, the overshoot levels are lower at rise times less than $1 \mu\text{s}$. Another important conclusion resulting from these curves is that varistor clamping voltages above 600 kV provide an ultra-fast rise time and at the same time very low overshoot levels. This is explained from the fact that the varistor branches operate in the leakage region for voltages lower than the clamping voltages $V_{\text{var},x}$ and, as a result, the network in Fig. 4a) mainly consists of the parasitic inductance L_t and capacitance C_t as well as the resistor R_{extra} at the output and the gun. The damping network improves the overshoot, but it also inserts a delay (i.e. it increases the rise time) as it is essentially a RC circuit in parallel to the transformer secondary winding and therefore, the optimal clamping voltages $V_{\text{var},x}$, when each varistor branch would be "activated", need to be identified. For this, different curves are plotted in Fig. 4b) with a focus on clamping voltages higher than 600 kV. There, it can be seen that there is an optimal set of varistor clamping voltages (red dashed line) for which low rise times and low overshoots can be achieved at the same time. However, even at the $1 \mu\text{s}$ rise time limit, the overshoot is around 3%, which remains outside of the value required by the application (1%). Consequently, three and four varistor branches are also investigated in Fig. 7c) and d). By adding a third varistor and a fourth branch significant lower overshoot levels are observed and the 1% overshoot is feasible for both of these cases. The red dashed curves denote again the clamping voltages where minimum rise times and overshoots can be achieved.

By the inspection of how the DN parameters, i.e. the quantities R_x , C_x and R_{extra} relate to each other around the rise time limit for the cases $N_b = 1$ and $N_b = 2$, one can further reduce the ranges of the parameters of interest. This helps to reduce the intervals of the parametric sweep, especially when a third and a fourth varistor branch are inserted, which increases the computational time significantly.

Although the obtained curves given in Fig. 7 do provide a relation between two important transient characteristics of the pulse, i.e. the rise time and the overshoot, they do not give an insight regarding the settling time of the pulse, a characteristic which is equally or even more significant than the rise time itself. This is because a high settling time means a long exposure of the gun to a high voltage, which could potentially lead to a breakdown of

Table V: Varistor parameters

Parameter	Value
C_{var}	250 pF
R_{off}	1000 M Ω
L_{lead}	32 nH
$V_{\text{clamp}} (8/20 \mu\text{s})$	1.65 kV
h	25.4 mm
d	10 mm
t_w	0.81 mm

Table VI: Considered boundaries for the DN parameters

Parameter	Value
R_x	$0.02 \text{ k}\Omega \leq R_x \leq 5 \text{ k}\Omega$
C_x	$50 \text{ nF} \leq C_x \leq 1 \mu\text{F}$
$V_{\text{var},x}$	$350 \text{ kV} \leq V_{\text{var},x} < 700 \text{ kV}$
R_{extra}	$0.087 R_{\text{gun}} \leq R_{\text{extra}} \leq 0.2 R_{\text{gun}}$

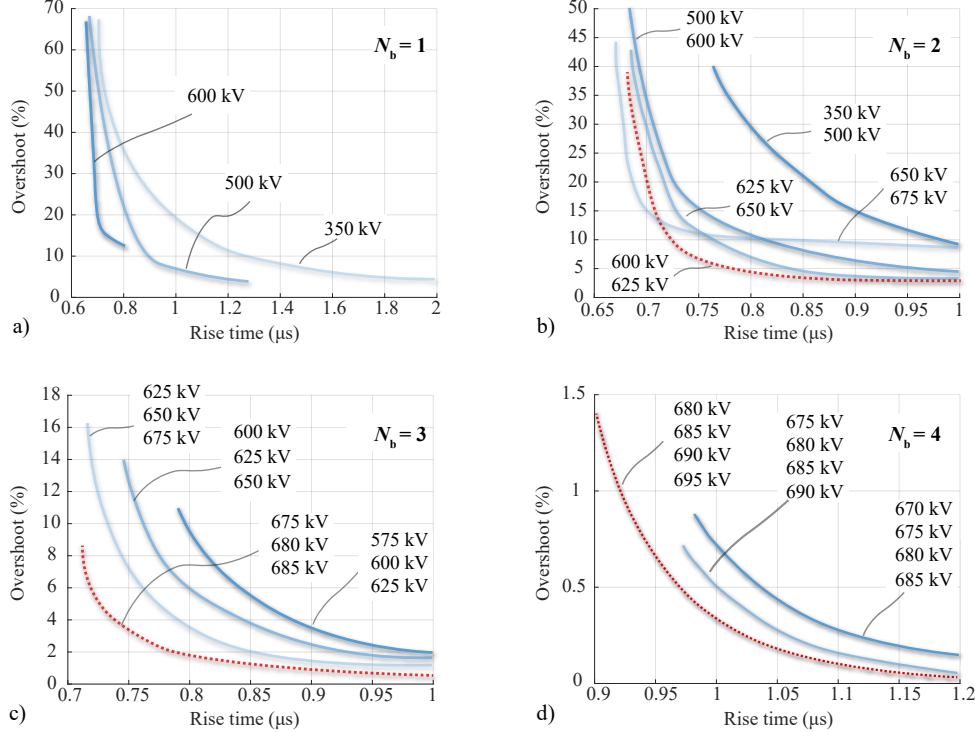


Fig. 7: Dependency between rise time & overshoot for different number N_b of varistor branches in parallel: a) $N_b = 1$, b) $N_b = 2$, c) $N_b = 3$, d) $N_b = 4$. The red dashed lines indicate the clamping voltages, which offer minimum rise times and overshoots at the same time for each number of varistor branches.

the gun. Furthermore, even though the rise time and the overshoot might fulfill the requirements, the pulse might not lie within the *FTS* band in an acceptable settling time. Therefore, it is interesting to discuss the dependencies between the settling time and the other two transient characteristics, i.e. the rise time and the overshoot, for damping networks with two, three and four branches in parallel. For this, design points are selected on the red dashed curves of Fig. 7b) and c), which are found to be the clamping voltages offering optimal combinations of rise times and overshoots. So far, the red curves are limited until the rise time limit of 1 μ s, but now they are extended further in order to find the optimal settling times as well. The optimal design points are summarized in Table VII for a 0.1% *FTS*. Of course, there are numerous designs that lead to settling times less than 5 μ s with different combinations of R_x , C_x and R_{extra} even outside the considered DN parameters boundaries. However, the values of the DN parameters should be small and therefore, designs with minimum settling times and minimum DN parameters values at the same time are listed in Table VII. From this table, it is clearly visible that a settling time of less than 5 μ s can already be achieved with 2 varistor branches, but the rise time remains higher than 1 μ s. However, three varistor branches in parallel result in an improved pulse performance with a shorter settling time of 2.44 μ s, a rise time of 1.07 μ s and a negligible overshoot. In case four branches are inserted, the settling time drops to 2.33 μ s with a rise time of less than 1 μ s, bringing the pulse to completely meet the imposed specifications. The resulting pulse shape (dark blue) for the case of four varistor branches is depicted in Fig. 8a) whereas in Fig. 8b) a zoomed illustration of the pulse after its settling and until the end of the flat-top is shown. In Fig. 8c), a CAD illustration of the transformer geometry for the selected design point is shown.

In the same table, the pulse shape and the DN parameters for different oil types and maximum allowed field values E_{th} are shown, in order to investigate the influence of these two quantities. For this, the optimization procedure is set to assume mineral oil, having a relative permittivity of 2.2 and two different threshold E_{th} values of 20 kV mm $^{-1}$ and 25 kV mm $^{-1}$. For these cases, only the optimal $V_{\text{var},x}$, which have been identified above, for two and three branches are considered. Also, a design point at the knee of the respective Pareto fronts is chosen. With a higher E_{th} and using mineral oil, which has a lower permittivity compared to the synthetic ester oil Midel 7131, a Pareto front with lower leakage inductance/parasitic capacitance sets results. Due to the smaller parasitics, shorter rise and settling times occur as it is shown in Table VII for two and three branches. In case a higher E_{th} and mineral oil are allowed, significant improvements can be achieved in terms of the rise and settling time, and with three varistor branches the pulse has transient characteristics, which comply with the specifications. The best achievable pulse shape is in the case of mineral oil with an $E_{\text{th}} = 25 \text{ kV mm}^{-1}$, where a 0.93 μ s rise time is achieved with an ultra-fast settling time of 2.1 μ s. The pulse shape for this case (light blue) is given in Fig. 8a) and Fig. 8b).

Table VII: DN & pulse shape parameters for different number of varistor branches and for different oil types and E_{th} values

Oil type/ E_{th} (kV/mm)	$V_{var,1}$ (kV)	$V_{var,2}$ (kV)	$V_{var,3}$ (kV)	$V_{var,4}$ (kV)	R_1 (Ω)	R_2 (Ω)	R_3 (Ω)	R_4 (Ω)	C_1 (nF)	C_2 (nF)	C_3 (nF)	C_4 (nF)	R_{extra} ($k\Omega$)	t_{rise} (μs)	$t_{settling}$ (μs)	os (%)
Midel/18	600	625	—	—	440	430	—	—	900	850	—	—	0.1 R_{gun}	1.49	2.86	0.04
Mineral/20	600	625	—	—	530	540	—	—	700	700	—	—	0.1 R_{gun}	1.42	2.6	0.049
Mineral/20	600	625	—	—	510	520	—	—	700	700	—	—	0.1 R_{gun}	1.38	2.55	0.049
Midel/18	675	680	685	—	8	6.5	5.5	—	900	950	950	—	0.1 R_{gun}	1.07	2.44	0.05
Mineral/20	675	680	685	—	80	81	81	—	800	800	750	—	0.1 R_{gun}	0.94	2.13	0.048
Mineral/25	675	680	685	—	60	65	65	—	600	700	600	—	0.1 R_{gun}	0.93	2.1	0.049
Midel/18	680	685	690	695	50	34	32	35	900	900	900	900	0.15 R_{gun}	0.98	2.33	0.049

3.4 Computational Effort of the Design Procedure

After the results section, the computational effort that is needed for the complete design procedure is discussed. All the steps of the design procedure are implemented on a server-based computer with a 32-core processor at 2.95 GHz (2 processors). For instance, for the case of Midel oil with $E_{max} = 18 \text{ kV mm}^{-1}$ the elapsed time of the transformer design part was around 4.5 hours and the optimization operates in a brute-force mode. The 3D FEM simulations (electrostatic and magnetostatic) need around 3 hours to finish. This computational time can be further decreased if someone is not interested to investigate the interaction between the 2 secondary windings inside the core window and, as a result, additional symmetry planes can be used to reduce the transformer and tank geometry. The most computationally demanding step is the damping network design. There, hundreds of thousands of iterations are needed to produce the rise time versus overshoot curves and identify, at the end, the optimal clamping voltages of each varistor branch. The elapsed time for two varistor branches and one set of clamping voltages was approximately 24 hours. For the case of three and four varistor branches, where the computational effort rises dramatically for the chosen parameter range, the designer should observe the relation between R_x , C_x in one and two varistor branches, and shrink the intervals of the DN parameters.

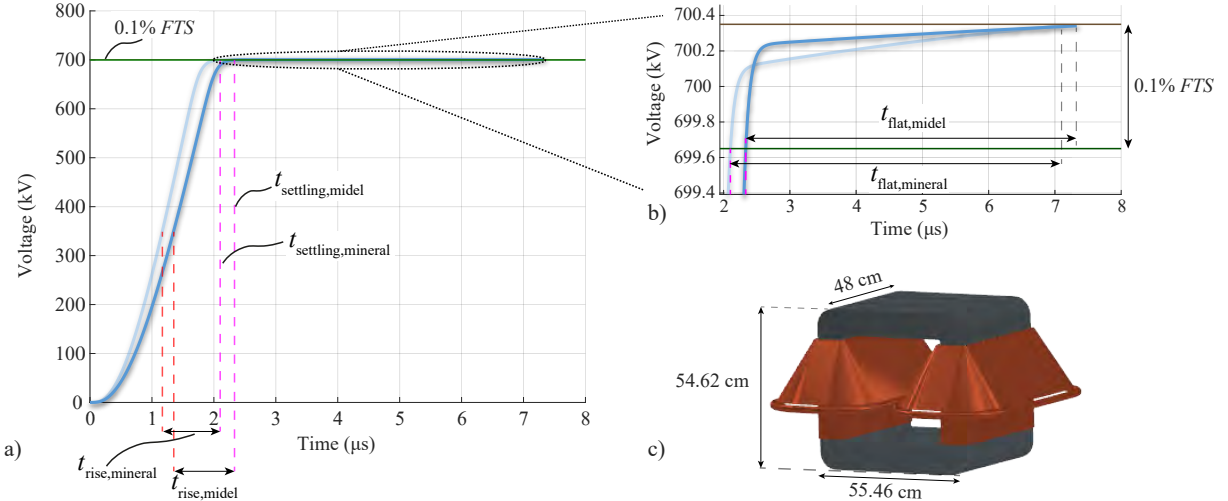


Fig. 8: a) Pulse shapes for Midel 7131 transformer oil, $E_{th} = 18 \text{ kV mm}^{-1}$ and four varistor branches (dark blue), and mineral oil with $E_{th} = 25 \text{ kV mm}^{-1}$ and three varistor branches (light blue). For the case of MIDEL 7131 oil, the pulse has a rise time of $0.98 \mu s$ and an overshoot of 0.049% . The $0.1\% FTS$ limit can be reached within a settling time of $2.33 \mu s$. For the case of mineral oil, the pulse shows a rise time of $0.93 \mu s$ and an overshoot of 0.049% . The $0.1\% FTS$ limit can be met within a settling time of $2.1 \mu s$. b) Zoomed view of the pulses after their settling and until the $5 \mu s$ flat-top interval finishes. The pulse lies safely inside the FTS limits until the $5 \mu s$ flat-top interval ends. c) CAD illustration of the transformer geometry for the selected design point with MIDEL 7131 transformer oil and an $E_{th} = 18 \text{ kV mm}^{-1}$.

4 Conclusion

In this paper, an extended systematic design procedure is presented, which combines the optimal design of the transformer and the optimal design of a damping network for transformer-based solid-state modulators. To validate the performance of the optimization routine, it is applied to the specifications of the CARM modulator system. The procedure has improved models regarding the insulation design of the transformer and the analytical calculation of the transformer parasitics as well as a detailed damping network modeling. By applying the optimization procedure, different transformer and damping network designs are proposed for the CARM modulator system, which manage to comply with the strict specifications imposed by the application. The optimization procedure is general and it can be adopted to arbitrary rise time ranges and various pulse lengths leading to a transformer with a compact volume.

References

- [1] J. Holma and M. J. Barnes, “The prototype inductive adder with droop compensation for the CLIC kicker systems,” *IEEE Trans. on Plasma Science*, vol. 42, no. 10, pp. 2899–2908, 2014.
- [2] D. Gerber and J. Biela, “Design of an ultraprecise 127-MW/3- μ s solid-state modulator with split-core transformer,” *IEEE Trans. on Plasma Science*, vol. 44, no. 5, pp. 829–838, May 2016.
- [3] S. Blume, M. Jaritz, and J. Biela, “Design and optimization procedure for high-voltage pulse power transformers,” *IEEE Trans. on Plasma Science*, vol. 43, no. 10, pp. 3385–3391, Oct. 2015.
- [4] S. Candolfi, P. Viarouge, D. Aguglia, and J. Cros, “Hybrid design optimization of high voltage pulse transformers for klystron modulators,” *IEEE Trans. on Dielectrics and Electrical Insulation*, vol. 22, no. 6, pp. 3617–3624, 2015.
- [5] M. Jaritz and J. Biela, “System design and measurements of a 115-kV/3.5-ms solid-state long-pulse modulator for the european spallation source,” *IEEE Trans. on Plasma Science*, vol. 46, no. 10, pp. 3232–3239, Oct. 2018.
- [6] I. Spassovsky, “From research and design work toward the realization of CARM source at ENEA,” in *44th Intern. Conf. on Infrared, Millimeter, and Terahertz Waves (IRMMW-THz)*, 2019.
- [7] S. Stathis and J. Biela, “Optimal design of a transformer-based solid-state pulse modulator with a damping network for ultra-fast rise times,” in *European Conf. on Power Electronics and Applications (EPE ECCE Europe)*, 2021.
- [8] G. V. N. Bezerra *et al.*, “Evaluation of surge arrester models for overvoltage studies,” in *ICHVE International Conf. on High Voltage Engineering and Application*, 2014.
- [9] CIGRE, “Guide for the development of models for HVDC converters in a HVDC grid,” 2014.
- [10] T. Hagiwara *et al.*, “A metal-oxide surge arrester model with active V-I characteristics,” in *Electrical Engineering in Japan*, vol. 121, 1997.
- [11] D. Bortis, J. Biela, G. Ortiz, and J. W. Kolar, “Design procedure for compact pulse transformers with rectangular pulse shape and fast rise times,” in *IEEE Intern. Power Modulator and High Voltage Conf.*, 2010, pp. 298–302.
- [12] H. Singer, H. Steinbigler, and P. Weiss, “A charge simulation method for the calculation of high voltage fields,” *IEEE Trans. on Power Apparatus and Systems*, vol. PAS-93, no. 5, pp. 1660–1668, 1974.
- [13] D. Bortis, “20 MW halbleiter-leistungsmodulator-system,” Ph.D. dissertation, ETH Zürich, 2009.
- [14] S. Candolfi, S. Blume, D. Aguglia, P. Viarouge, J. Biela, and J. Cros, “Evaluation of insulation systems for the optimal design of high voltage pulse transformers,” in *IEEE Intern. Power Modulator and High Voltage Conf. (IPMHVC)*, 2014, pp. 557–560.
- [15] Q. Liu, “Electrical performance of ester liquids under impulse voltage for application in power transformers,” Ph.D. dissertation, The University of Manchester, 2011.
- [16] J. Biela, “Optimierung des electromagnetisch integrierten serieng-parallel resonanzkonverters mit eingeprägtem ausgangsstrom,” Ph.D. dissertation, ETH Zürich, 2005.
- [17] M. S. Blume, “Highly efficient pulse modulator system with active droop compensation for linear colliders,” Ph.D. dissertation, ETH Zürich, 2016.
- [18] R. Schlesinger and J. Biela, “Analytical triple-2D leakage inductance model of cone winding matrix transformers,” in *23rd European Conf. on Power Electronics and Applications (EPE ECCE Europe)*, 2021.
- [19] S. Blume and J. Biela, “Optimal transformer design for ultraprecise solid state modulators,” *IEEE Trans. on Plasma Science*, vol. 41, no. 10, pp. 2691–2700, 2013.
- [20] Littelfuse, “Littelfuse varistors-basic properties, terminology and theory,” 1999.
- [21] N. Kularatna *et al.*, “Design of protection systems,” 2018.
- [22] F. Hohmann and M.-M. Bakran, “Impacts on the current distribution of metal oxide varistors for overvoltage protection in IGBT modules,” in *European Conf. on Power Electronics and Applications (EPE ECCE Europe)*, 2017.